FULL PAPER

Phase Transition Induced Synthesis of Layered/Spinel Heterostructure with Enhanced Electrochemical Properties

*Yi Pei, Cheng-Yan Xu, Yu-Chen Xiao, Qing Chen, Bin Huang, Bin Li, Shuang Li, Liang Zhen, and Guozhong Cao**

A one-step synthesis of Li-rich layered materials with layered/spinel heterostructure has been systematically investigated. The composites are synthesized by a polyol method followed with an annealing process at 500–900 °C for 12 h. A spinel to layer phase transition is considered to take place during the heat treatment, and the samples obtained at different temperatures show diverse phase compositions. An "Li-rich spinel phase decomposition" phase transition mechanism is proposed to explain the formation of such a heterostructure. The electrochemical properties of the heterostructure are found to be associated with the ratio of spinel to layer phases, the leach out of rock salt phase, and the change of crystallinity and particle size. Product with improved cyclic and rate performance is achieved by annealing at 700 °C for 12 h, with a discharge capacity of 214 mA h g^{-1} remaining at 0.2 C after 60 cycles and discharge capacity of about 200 mA h g^{-1} at 1 C.

1. Introduction

With the rapid steps of pushing the chemical energy storage devices, especially rechargeable alkali-ion batteries into the application in consumer electronics, large-scale smart grids, and electrical vehicles, cathodes with high energy density are considered to be the primary bottleneck.[1–4] In this context, the layered lithium-rich transition-metal oxides, noted as $xLi_2MnO_3\cdot(1–x)LiMO_2$ (LLO), have attracted broad interest.[5] With the average discharge voltage of about 3.5 V and a high specific capacity of 250 mA h g^{-1} or more, the energy density of LLO can reach up to 900 Wh kg^{-1}, much higher than that of commercial cathodes (560 W h kg^{-1} for layer-type $LiCoO_2$ and 580 W h kg^{-1} for olivine-type $LiFePO_4$), respectively.[6,7] Although the energy density is attractive, LLO suffers from several drawbacks including intrinsic low lithium diffusion kinetics and significant capacity fade, which restrict its practical applications.[8] In contrast, as typical high-rate cathode materials, spinel structure cathode materials exhibit faster electrical and ionic conductivities but low capacities.[9–11] To satisfy the application demand, the combination of the superiority of these two materials has attracted extensive interest in recent years.

By varying lithium contents with a fixed Mn:Ni ratio of 3:1, composites consisting of different ratios of spinel oxides and LLO were successfully synthesized, and the composites showed better electrochemical properties than that of single-phase LLO after 30 cycles.[12,13] As a typical method, intentional surface coating was introduced to prepare composite of LLO and spinel oxides. Wu et al. used an ex situ "dip and dry" method to introduce a thin layer of $LiNi_{0.5}Mn_{1.5}O_4$ onto the surface of LLO, and the encapsulated structure with LLO core and $LiNi_{0.5}Mn_{1.5}O_4$ shell exhibited excellent rate performance with a discharge capacity of 189.5 mA h g^{-1} at 10 C and capacity retention of 90.9% after 30 cycles.[14] Other methods, such as surface treatment[15–18] and doping[19,20] were also employed to design such layer/spinel composite, and all the modified products delivered highly improved cycle stabilities and rate properties. However, most of these reports involved tedious synthesis process and impurity phases are easily introduced in the subsequent modification process.[21]

Recently, several research groups obtained LLO/spinel heterostructure through one-step strategy with excellent electrochemical properties. For example, Luo et al. synthesized spinel-layered Li-rich Li—Mn—Co—O microspheres through solvothermal-precursor method.[22] By controlling the calcination temperature, small amounts of spinel phase were obtained as an impurity phase, and the products with moderate content of spinel phase demonstrated superior properties. Using a one-step solvothermal method, Deng et al. obtained LLO/spinel heterostructure with excessive Li source as well.[23] They pointed out that the calcination duration would influence the ratio of LLO to spinel phase, and the products with moderate content of spinel phase displayed the best properties. Although all of these researches successfully achieved spinel/layer structure with improved electrochemical properties, the formation mechanism of LLO/spinel heterostructure remains unclear, and the role of such heterostructure is obscure. Controlled synthesis of LLO/spinel heterostructure with desired electrochemical properties is still under challenge.

In the present study, spinel/LLO heterostructure with controlled phase compositions and morphologies were synthesized through a facile polyol method followed with subsequent

Dr. Y. Pei, Dr. B. Huang, Dr. B. Li, Dr. S. Li, Prof. G. Cao
Department of Materials and Engineering
University of Washington
Seattle, WA 98195-2120, USA
E-mail: gzcao@u.washington.edu
Dr. Y. Pei, Prof. C.-Y. Xu, Dr. Y.-C. Xiao,
Dr. Q. Chen, Prof. L. Zhen
School of Materials Science and Engineering
Harbin Institute of Technology
Harbin 150001, China

DOI: 10.1002/adfm.201604349

calcination. The phase composition, crystal structure, and oxidation state of the transition metal ions were studied, and based on these characterizations, an "Li-rich spinel phase decomposition" mechanism was proposed to explain the formation of such heterostructure. By changing the annealing temperature, the synergistic effect of the crystallinity, morphology, and the phase composition on the electrochemical properties were discussed. The products with 5.8% spinel phase obtained at moderate temperature exhibited superior electrochemical performance. This new strategy can be utilized in the further research of spinel/LLO heterostructure with controlled composition and electrochemical properties.

2. Results and Discussion

2.1. Morphology and Crystallinity of Spinel/LLO Heterostructure

The morphologies of calcination temperature-resolved samples were characterized by scanning electron microscope (SEM) and shown in **Figure 1**. For the samples calcined at temperatures from 500 to 700 °C, the particle size increases from about 20 to 80 nm; microsized particles (1–3 μm) were obtained at a calcination temperature of 800 °C. It should be noted that the particles in L-700 and L-800 seem to have a polyhedral characteristic with sharp edges. From the research on the surface energy of LLO by Wei et al., morphology is controlled by the low surface energies of the (001) plane: 0.937 J m^{-2} and (010) plane: 1.467 J m^{-2}, which determine the specific facets of the equilibrium crystals.[24] The particle size further increases to about 5 μm when calcined at 900 °C, accompanied by increased aggregation and porosity. Such aggregation should be caused by the sintering effect at high temperature, while the porosity is likely to be caused by the volatilization of Li, which may result in some structure change and tensile stress on the surface.[25]

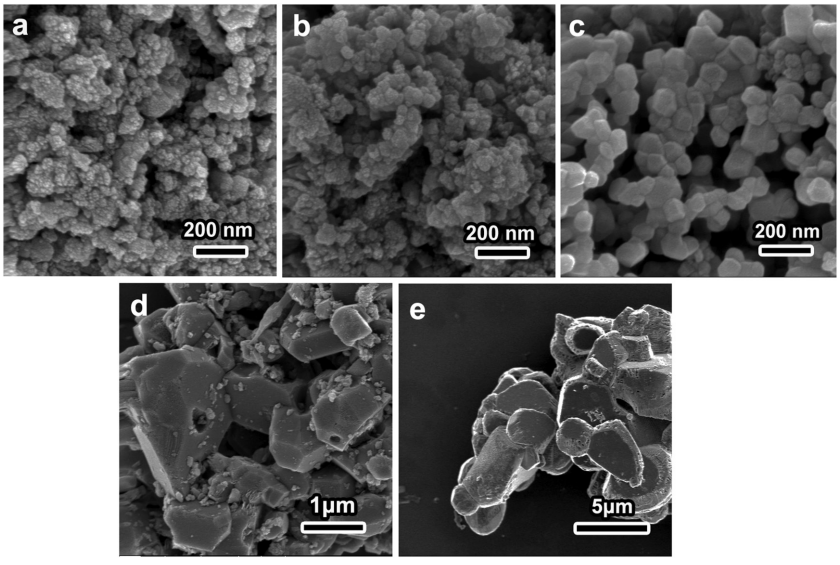

Figure 1. SEM images of the products calcined in air under different temperatures for 12 h: a) 500 °C; b) 600 °C; c) 700 °C; d) 800 °C; e) 900 °C. The ramping rate is 3.5 °C min^{-1} and samples are cooled naturally in the oven.

High-resolution TEM (HRTEM) characterization was further carried out to investigate the crystal structure of the samples. HRTEM images of L-500 and L-700, as representative results, are shown in **Figure 2**. The HRTEM image of L-500 shown in Figure 2a displays two sets of lattice fringes, suggesting the coexistence of two phases. Upon fast Fourier transform (FFT) of the regions marked by dash squares, one set of lattice fringes has a *d*-spacing of 0.29 and 0.25 nm, corresponding to (220) and (311) planes of spinel phase ($Fd\bar{3}m$), respectively. The other one has a *d*-spacing of 0.14 nm, corresponding to (110) plane of layer phase ($R\bar{3}m$). The spinel and layer phase were combined with a clear phase boundary marked by the dashed line. In the HRTEM image of L-700, the external region marked by the dashed line displays a different lattice fringe from the inside region, suggesting the coexistence of two phases instead of twinning.[26] FFT-filtered HRTEM images shown in the insets indicate that the lattice fringes of the inner region have a *d*-spacing of 0.47 and 0.41 nm, corresponding to (002) and ($\bar{1}11$) planes of layer phase (*C2/m*), while the external region has a *d*-spacing of 0.24 and 0.20 nm, corresponding to (222) and (400) planes of spinel phase, respectively. The thickness of the spinel layer is about 5 nm, indicating that the spinel phase may only occupy a relatively small portion of the entire particle. The HRTEM image of L-900 was shown in Figure S1 in the Supporting Information, and there also existed two domains with different lattice fringes corresponding to spinel and layered phases, respectively.

From the HRTEM results, it seems that the obtained particles are likely to be composed of layer and spinel phase. In order to estimate the constitution of each product, structural characterization was carried out by means of XRD. The patterns of sample calcined at different temperatures **(Figure 3a)** indicate that the major phases of all the products are LLO and spinel. LLO exhibits the characteristic of the layered α-$NaFeO_2$ structure with the combined pattern of Li_2MnO_3 (JCPDS No.: 27–1252, space group: *C2/m*) and $LiNi_{0.5}Mn_{0.5}O_2$ (JCPDS No.: 74–8073, space group: $R\bar{3}m$), while spinel phase (JCPDS No.: 80–2162, space group: $Fd\bar{3}m$) shows slight shift of diffraction peaks when compared to LLO. As shown in Figure 3a, the phase composition varies with annealing temperatures. In the XRD pattern of L-500, the weak peaks around 21° indexed to the $LiMn_6$ superstructures suggested the existence of layered Li-rich phase.[27] However, in the amplified regions of 18°–19.5° and 35°–39° shown in Figure 3b, the peaks fit better with the spinel phase, which can be assigned to the reflections of (111) and (311) planes of spinel phase, respectively. The differences in position and intensity of peaks in 18°–19.5° and 35°–39° are indicative of the continuous phase composition change. With the exception of L-800 and L-900, the peak around 19° gradually moved to the low angle with increased temperature; meanwhile, the peak assigned to the (101) reflection of LLO increased and the peak assigned to the (311)

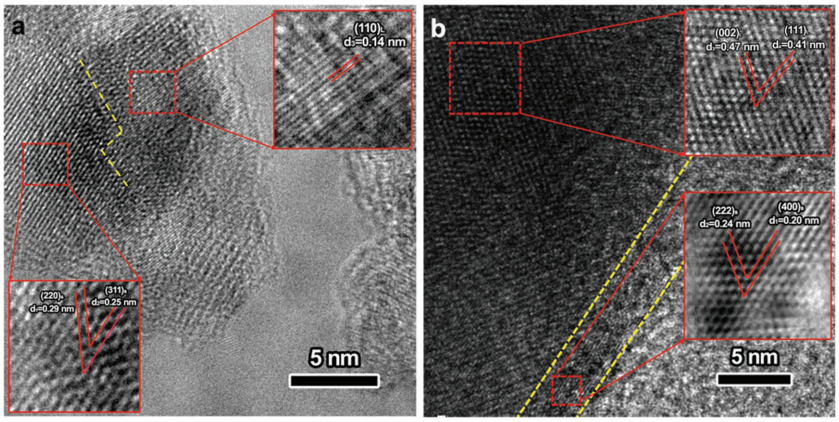

Figure 2. HRTEM images of the samples calcined in air under different temperatures for 12 h: a) 500 °C; b) 700 °C. The insets marked by red square are the FFT-filtered images of selected areas in the dashed square. The interface of two phases is marked by dashed lines.

reflection of spinel phase decreased. Considering the fact that when the temperature was raised from 500 to 700 °C, both the crystallinity of layered and spinel domains should increase, and the increased domain size would result in the narrowed peak width rather than the change of intensity. These peak changes would be influenced by the content of each phase, suggesting the content change of spinel and LLO phases with the increasing temperature until 700 °C.[28] However, the situation in L-800 and L-900 is different from that in low-temperature samples. Reflection referring to the (111) plane of spinel phase reappeared in the patterns of L-800 and L-900, and the intensity of both the (111) and (311) characteristic peaks of spinel phase increased gradually, suggesting the increased content of spinel phase. To compare the component of Li_2MnO_3, low-scan speed XRD measurements from 16° to 23° was carried out with the scan speed of 0.8° min^{-1} for L-500, L-600, and L-700. As demonstrated in Figure S2 in the Supporting Information, the relative intensity of superlattice reflections is the highest in L-700, which may represent that more Li ions have been inserted into the transition layer in LLO,[29] and is possibly indicative of increased content of LLO in L-700. In addition, two extra peaks appeared at 44.1° and 63.9° in samples L-800 and L-900, representing the existence of rock salt structure $Li_xNi_{1-x}O$, which is formed by the reaction in Equation (1).[30] The leaching out of $Li_xNi_{1-x}O$ will lead to the decrease of the nickel content in spinel phase.[30]

$$LiNi_{0.5}Mn_{1.5}O_4 \leftrightarrow \alpha Li_xNi_{1-x}O + \beta LiNi_{0.5-\gamma}Mn_{1.5+\gamma}O_4 + \gamma O_2 \quad (1)$$

Further Rietveld refinements with software package GSAS and the EXPGUI interface were carried out to determine the precise content of each phase in the products. Based on the primary XRD analyses, the phase composition in L-500, L-600, and L-700 is assumed to be a mixture of LLO and $LiNi_xMn_{2-x}O_4$, while the phase composition in L-800 and L-900 is mixture of LLO, $LiNi_xMn_{2-x}O_4$, and $Li_xNi_{1-x}O$. Refined profiles of each sample and the detailed parameters are shown in Figure S3 in the Supporting Information, and the content of spinel phase in each sample is displayed in Figure 3c. The spinel content is highest in L-500 with a mass fraction of 66.7%; with further increased annealing temperature, that content first decreased to 5.8% in L-700 and then gradually increased to 21.5% in L-900. Such composition change, which is associated with the annealing temperature, suggested that a spinel-layer-spinel phase transition is likely to take place during the calcination process. The layer-spinel phase transition at high temperature (≥800 °C) has been reported in literature and is considered to be caused by the loss of Li through volatilization.[31,32] However, no mechanism has been proposed to explain the spinel to LLO phase transition, even though similar heterostructure has also been observed in literature.[22,23] Considering the fact that spinel phase with excessive Li will decompose to Li_2MnO_3,[33] an analogous phase transition from spinel to LLO phase is likely to take place at relative low temperature (500–700 °C) in the present study.

2.2. Thermal and Composition Analysis

Thermogravimetric (TG) test was carried out in air with a ramping rate of 5 °C min^{-1}, and the curve in **Figure 4** showed that there is a weight loss of 6.8% below 200 °C, most likely due to the removal of absorbed water.[34] The subsequent 12.6% weight loss between 200 and 280 °C could be attributed to the pyrolysis of residential organic functional groups such as glycerol.[35] There appears a sharp weight loss of 33.5% between 280 °C and 307 °C, and such a weight loss seems to be attributable to the decompositions of acetates.[36–38] The fourth segment between 307 °C and 500 °C shows a flat curve with a small and mild weight change. XRD results showed that the product obtained at 500 °C are the composite of spinel phase and LLO, so this 4.7% weight loss is probably referred to the formation of crystalline spinel phase and LLO companied with gaseous byproduct releasing such as CO_2.[39,40] There is an even more flat curve in the last region between 500 and 900 °C; the approximately linear curve has only 2.4% weight loss. Such a weight loss has been observed in both spinel phase[41] and LLO[42,43] and were generally considered as the evolution of O_2 and Li, which will change the oxidation state of transition metal cations.[12]

The oxidation state of the transition metal cations changes with the phase transition, so high-resolution X-ray photoelectron spectroscopy (XPS) scans and the fitted curves, emphasizing the Mn 3s and Ni $2p_{3/2}$ spectra of the calcination temperature-resolved samples, were collected and shown in **Figure 5** to provide the surface information of each layered/spinel heterostructure. As described in literature,[44] the splitting energy between the main peak and its satellite in Mn 3s spectra is rather sensitive to the Mn valence state. As reported in literature,[45] Mn 3s spectra is differentiated and imitated with two pairs of peaks: one pair has a restricted splitting energy of 5.5 eV, representing the binding energy of Mn^{3+}; the other pair has restricted splitting energy of 4.6 eV, representing the binding energy of Mn^{4+}. According to the percentage of the

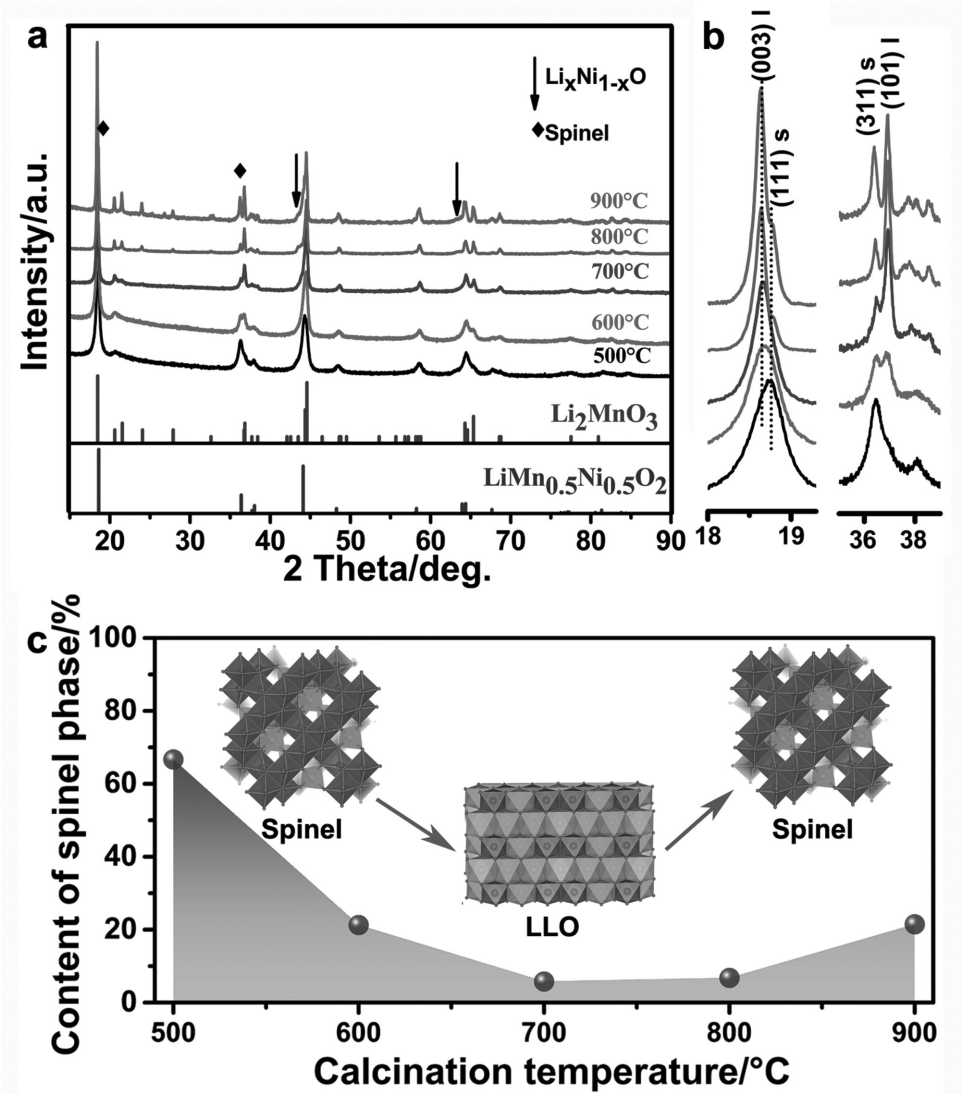

Figure 3. a) XRD patterns of the products calcined at different temperatures in air for 12 h. The standard Bragg position of Li_2MnO_3 and $LiMn_{0.5}Ni_{0.5}O_2$ are indicated. The peaks marked by arrows and rhombuses are the reflections originating from spinel phase ($LiNi_xMn_{2-x}O_4$) and rock salt phase ($Li_xNi_{1-x}O$), respectively. b) The amplified region of 18°–19.5° and 35°–39°. c) Rietveld refinement content of spinel phase in products calcined at different temperatures in air for 12 h. The crystal structures of $LiNi_xMn_{2-x}O_4$ and LLO are shown as insets in (c).

fitted peak area shown in Figure 5c, the content of Mn^{3+} on the surface calculated from the peak area is highest in L-500, which is about 27%. The decrease of Mn^{3+} peak area is qualitatively visible when the annealing temperature is raised from 500° to 700 °C, representing the reduced content of Mn^{3+} on the surface. It has been indicated that Mn ions are always existing in the form of Mn^{4+} in LLO[46] when no aliovalent element added,[47] but tend to exist as both Mn^{3+} and Mn^{4+} in the spinel phase $LiNi_xMn_{2-x}O_4$ when $x < 0.5$.[41] Thus, the reducing content of Mn^{3+} at the surface from L-500 to L-700 is possibly associated with the spinel to LLO phase change from 500 to 700 °C. Analogously, the further increased content of Mn^{3+} at the surface of L-800 and L-900 could also be associated with the formation of spinel phase at high temperature. The fitted curves of Ni $2p_{3/2}$ spectra in Figure 5b also manifest the coexistence of binding energy of Ni^{2+} (854.2 eV)[48] and Ni^{3+} (855.5 eV)[49] in the surface at all the analyzed specimens. The fitted peaks have comparable peak position and area in the spectra of L-500 and L-600, demonstrating almost no oxidation change of Ni on the surface. From the percentage of the fitted peak area, the content of Ni^{3+} progressively increased from L-700 to L-900. That oxidation change can be traced by the leaching out of $Li_xNi_{1-x}O$ phase as shown in the XRD pattern, and the content of $Li_xNi_{1-x}O$ in L-700 is too low to be detected by XRD. The O 1s spectra shown in Figure S4 in the Supporting Information reveal two types of O^{2-} coexisting in the products, belonging to the crystalline network (529 eV peak) and weakly absorbed surface species (531 eV peak),[50] and the peak area at 531 eV keeps increasing with increased temperature.

Inductively coupled plasma (ICP) analyses were carried out to further verify the chemical composition of each product. As shown in **Figure 6**, all of the analyzed specimens have almost

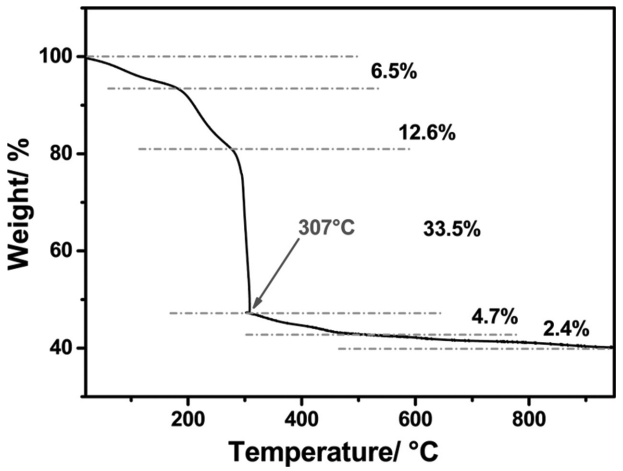

Figure 4. TG curve of the precursor. The test is carried out in air with the ramping rate of 5 °C min^{-1}. Different stages of weight loss are separated by dashed lines.

the same content of Mn and Ni; the ratio of Mn:Ni is 3:1. However, the Li content varies among the specimens; L-500 has the lowest Li content (0.763) and the Li content gradually increased to 1.193 in L-700. In L-700 and L-800, the ratio of Li:M (Mn + Ni) is approximately 1.5:1, which is the stoichiometric ratio of that in LLO, and the Li content further decreased to 0.949 in L-900. As the ratio of Li:M (Mn + Ni) is 1:2 in $LiNi_xMn_{2-x}O_4$ and 1.5:1 in LLO, such element content changes are in accordance with the former results that a spinel-layer-spinel phase transition may take place during the calcination process. It should be noted that for L-500 and L-600, the unreacted Li source would have been washed away after the calcining process.

2.3. Mechanism of the Phase Transition

The experimental results suggested that a spinel-layered-spinel phase transition occurred during the calcination process. Low-temperature treated specimen (500 °C) is dominated by the spinel phase, and a phase transition from spinel phase to LLO took place at temperatures between 500 and 700 °C. Specimen with the lowest content of spinel phase was obtained at 700 °C; higher temperature (800–900 °C) will volatilize Li and further increase the content of spinel. It should be noted that in most of the research reported so far, LLO was synthesized without the formation of intermediate phase; through methods such as sol–gel,[31] reverse microemulsion,[51] and co-precipitation,[39] LLO was detected to be directly formed with the consumption of precursors. Wang et al. observed the temperature-induced formation of layered-spinel structure, but it is more likely to be an immediate reaction at 850 °C as the spinel phase instantly vanished when the temperature increased from 800 to 850 °C.[52]

The formation of the heterostructure in the present study is likely due to an "Li-rich spinel phase decomposition" process. As shown in the TG curve, the precursor prepared by this polyol method decomposes and reacts at about 310 °C, and the weight is relatively stable after 500 °C, suggesting most of the organics are decomposed before 500 °C. Upon calcination at 500 °C for 12 h, the XRD pattern indicates that the product is predominated by spinel phase; although the Li source is excessive for LLO, only half of the raw Li source remained in the product obtained at 500 °C. Thus, it is hypothesized that spinel phase may be preferentially formed due to thermodynamics/dynamics restrictions, which hinder the excessive Li inserted into the lattice at such temperature. However, this process seems to be specifically dependent on the synthesis method and the precursor form. For example, for the carbonate and hydroxide precursors obtained by co-precipitation method,[39,53,54] it seems to be a one-step reaction with the precursor consumed and LLO generated. For precursors obtained by the polyol method in this research, however, it seems to be more likely a two-step reaction with the intermediate phase of spinel phase. With increasing temperature, more Li inserted into the products, as indicated by the ICP results and the content of layered structure increased. According to former research, when Li content is excessive for the spinel phase ($LiMn_2O_4$), Li-rich spinel phase ($Li_{1+x}Mn_{2-x}O_4$) would transform into Li_2MnO_3 and $Li_{1+x'}Mn_{2-x'}O_4$ ($x' < x$) at phase transition temperature, T_c, with the reaction shown in Equation (2).[28,33] Such phase transition is likely promoted by high Li content and temperature, and $Li_{1+x}Mn_{2-x}O_4$ finally decomposed to $LiMn_2O_4$ and Li_2MnO_3. LLO was detected to be the same structure with Li_2MnO_3 (*C2/m*) when lithium content is more than 1.15, and a two-phase mixture consisting of *C2/m* and $R\bar{3}m$ phases with a lower lithium content.[31] An analogous reaction (Equation (3)) can be established to explain the mechanism of the phase transition when annealing below 700 °C. Moreover, further increased spinel content at high temperature (≥800 °C) has been reported many times in previous research and is considered to be resulted from the Li volatilizing at high temperature.[6,31] A qualitative schematic illustration of the phase transition is shown in **Figure 7** to describe the formation of such layered/spinel heterostructure. The products obtained at low temperature (≤500 °C) may be composed by LLO and Li-rich spinel phase with the formula of $Li_{1+x_1}Ni_{x_2}Mn_{2-x_1-x_2}O_4$, and the later one is the main phase. Further increased temperature (>500 °C) leads to the decomposition of $Li_{1+x_1}Ni_{x_2}Mn_{2-x_1-x_2}O_4$ through the reaction in Equation (3), so the products obtained at 500–700 °C should be composed of $Li_{1+x'}Ni_{x_3}Mn_{2-x'-x_3}O_4$ ($x' < x_1$) and LLO phase, and the content of LLO gradually increased along with the increased temperature. Such reaction keeps moving, and the excessive Li would gradually compensate the Li in spinel phase until the excessive Li is exhausted at about 700 °C. Thus, as shown in Figure 7, the particle composed of LLO and small domains of spinel phase in L-700

$$Li_{1+x}Mn_{2-x}O_4 \leftrightarrow (1-z)Li_{1+x'}Mn_{2-x}O_4 + zLi_2MnO_3 + z/2O_2 \quad (2)$$

where $x' = (x - z)/(1 - z)$

$$\begin{aligned} &Li_{1+x_1}Ni_{x_2}Mn_{2-x_1-x_2}O_4 \\ &\quad + \gamma_1\left[\gamma_2 Li_2MnO_3 \cdot (1-\gamma_2)LiNi_{0.5}Mn_{0.5}O_2\right] \\ &\quad \leftrightarrow (1-z)Li_{1+x'}Ni_{x_3}Mn_{2-x'-x_3}O_4 \\ &\quad + \gamma'_1\left[\gamma'_2 Li_2MnO_3 \cdot (1-\gamma'_2)LiNi_{0.5}Mn_{0.5}O_2\right] + z/2O_2 \end{aligned} \quad (3)$$

where $x' = (x-z)/(1-z), x_3 = x_2/(1-z), \gamma'_1 = \gamma_1 + z$ and $\gamma'_2 = (z+\gamma_1\gamma_2)/(\gamma_1 + z)$

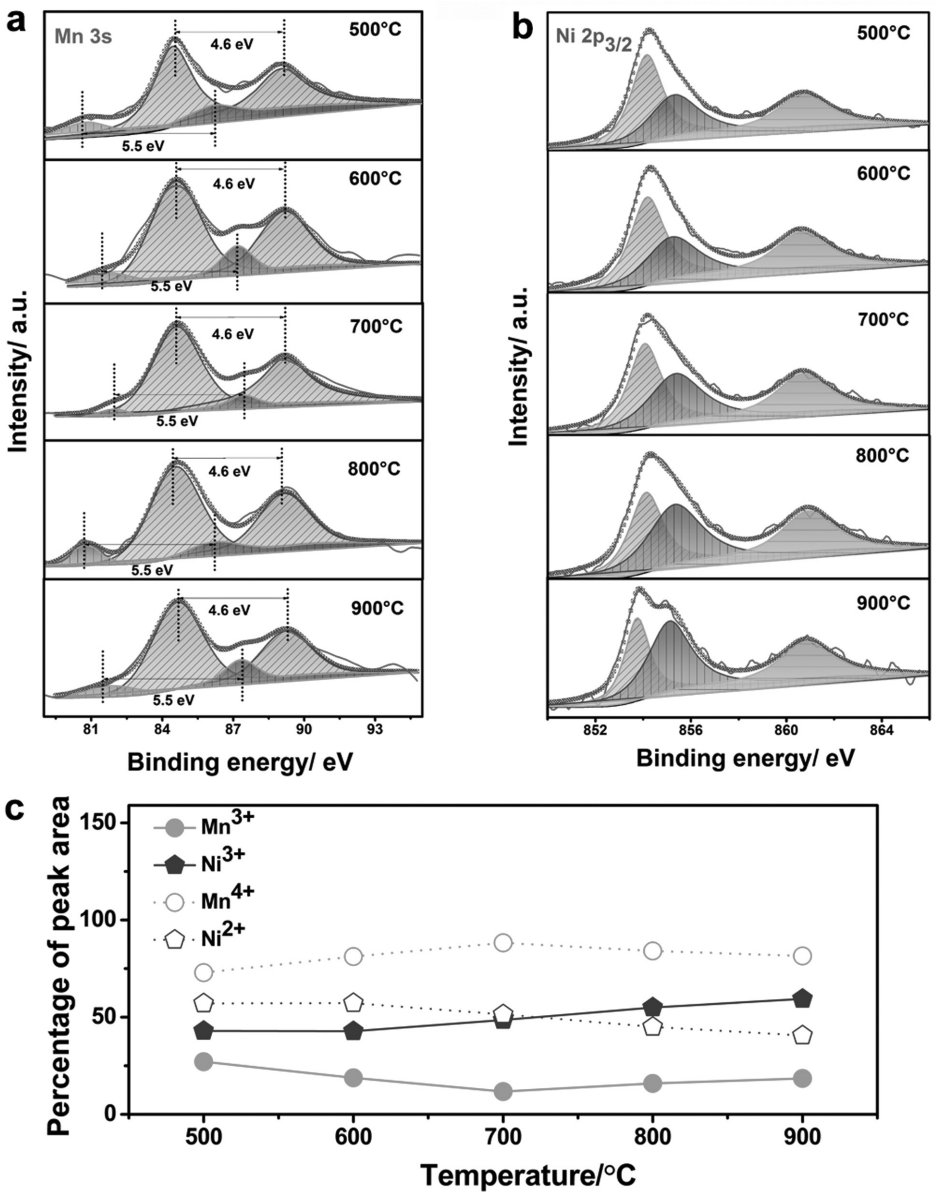

Figure 5. XPS spectra of the products calcined at different temperatures in air for 12 h. a) Mn 3s spectra. The peaks with splitting energy of 4.6 eV represent the binding energy of Mn^{4+}; the peaks with splitting energy of 5.5 eV represent the binding energy of Mn^{3+}. b) Ni 2p3/2 spectra and c) percentage of fitted peak area. The differentiated and imitated peaks are shown in different shading.

2.4. Electrochemical Properties

The electrochemical performances of the calcination temperature-resolved samples were tested by galvanostatic charge–discharge measurements at room temperature, with current density of 20 mA g^{-1} (0.1 C, 1 C = 200 mA g^{-1}) and work window of 2–4.8 V. The first and fifth charge–discharge profiles of the samples calcined at different temperatures are shown in **Figure 8**.

Sample L-500 exhibits an initial discharge capacity of 227 mA h g^{-1}, while the initial charge capacity is 202 mA h g^{-1}. The higher discharge capacity is attributed to the reversible, first-order spinel $Li[Ni_{0.5}Mn_{1.5}]O_4$ to rocksalt $Li_2[Ni_{0.5}Mn_{1.5}]O_4$ transformation with the displacement of lithium ions from tetrahedral to octahedral sites, corresponding to the plateau at 2.8 V.[12,55] During the discharge process, the plateaus of spinel phase at 4.7 and 2.8 V offer most of the capacities, and the section from 4.5 to 3 V with a slant curve is caused by the extracting of Li^+ from $LiMO_2$.[56,57] The initial discharge capacity is 172 mA h g^{-1} in the galvanostatic charge–discharge profile of L-600, which is lower than that of L-500. However, the discharge capacity of L-600 attributed to the slant curve from 4.5 to 3 V is slightly higher than in L-500. The decreased capacity is mainly ascribed to the reduction of plateaus at 4.7 and 2.8 V. Sample L-700 possesses a typical charge–discharge curve of LLO with a wide plateau at about 4.5 V during the charge process, referring to the removal of lithium ions and oxygen from Li_2MnO_3.[58] The small plateau at 4.7 V in the discharge curve witness the

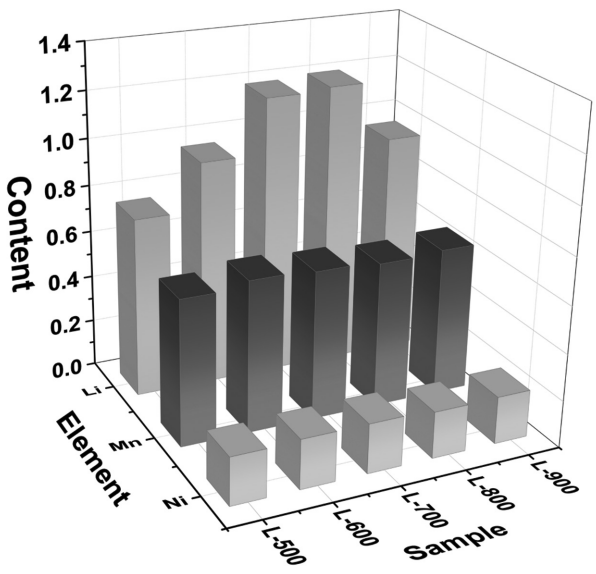

Figure 6. Chemical compositions measured by ICP for products calcined at different temperatures in air for 12 h.

existence of spinel phase. To have a quantitative comparison of these composites, galvanostatic discharge profiles of L-500 and L-700 with normalized capacity are performed. As shown in Figure S5 in the Supporting Information, there is about 0.51 normalized discharge capacity in the region from 4.5 to 4.8 V and 2.0 to 2.8 V of L-500, but only 0.17 in the discharge curve of L-700, indicating that the content of spinel phase in L-700 is much lower than that in L-500. The above results from the present study corroborate with earlier studies reported in the literature, for example, layered/spinel heterostructure with 50% spinel phase in the investigation by Park et al.[12] demonstrated similar profile with that of L-500 in our research, and the profile of L-700 is similar with that in the work by Chen et al.,[45] in which the content of spinel phase is about 7%. The initial discharge capacity of L-700 is 225 mA h g^{-1}, which is benefitted from the electrochemical activation of Li_2MnO_3 in the charge process. The first charge–discharge profiles of L-800 and L-900 manifest the risen content of spinel phase, as the plateaus at 4.7 and 2.8 V provide increased capacities, accompanied with decreased discharge capacities.

As shown in Figure 8b, the capacity of L-500 declines substantially after five cycles. Compared with the first charge–discharge curve of L-500, this capacity decay is mainly caused by the section of spinel phase, with the reducing of both plateaus at 4.7 and 2.8 V. L-600 has slight capacity decay in the fifth cycle, but from the discharge curve, the plateaus of spinel phase decreased as well. For these low-temperature specimens (≤600 °C), the reducing of plateaus at 4.7 and 2.8 V is supposed to be caused by the low crystallinity of low-temperature-formed spinel phase, as the low-crystallinity phase will easily lose the crystallinity during the repeated cycling processes.[15] Both L-700 and L-800 have about 20% higher discharge capacities in the fifth cycle than that in their initial cycle; the discharge capacities were 267 and 198 mA h g^{-1}, respectively. The phenomenon of this capacity increase has been reported constantly in previous research.[59,60] Ye et al., attributed such a phenomenon to the suppressed Li_2MnO_3 activation process affected by the formation of a small amount of spinel phase on the surface.[61,62] The discharge capacity of L-900 in the fifth cycle is also slightly higher than that in the first cycle due to the higher

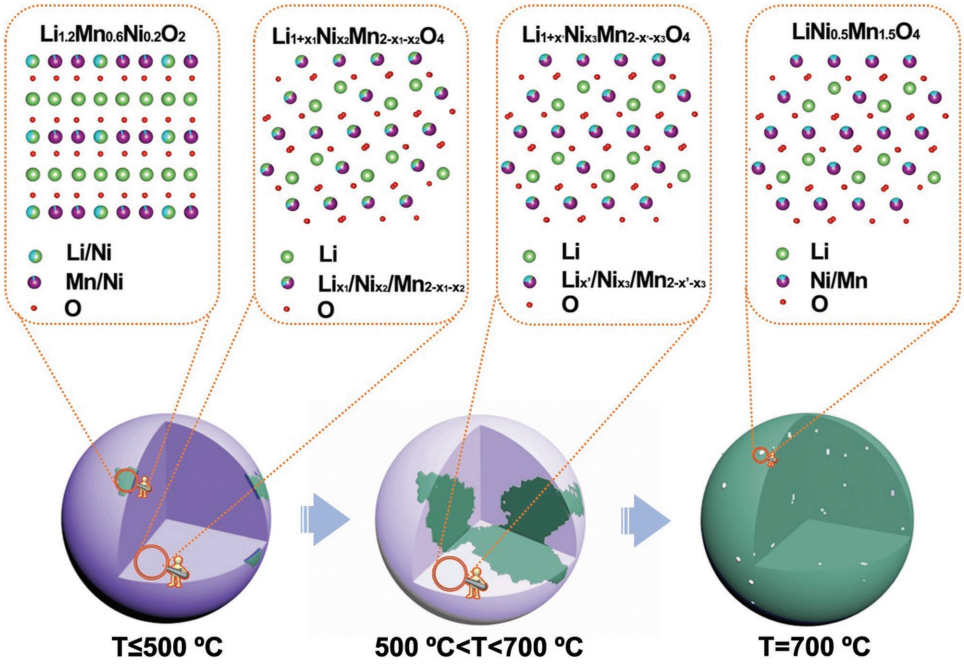

Figure 7. Qualitative schematic illustration of the formation of layered/spinel heterostructure. The phase colored as purple represent Li-rich spinel phase with high Li content ($0 < x_1$); the phase colored as gray violet represent Li-rich spinel phase with lower Li content ($0 < x' < x_1$); the phase colored as green represent LLO phase ($Li_{1.2}Mn_{0.6}Ni_{0.2}O_2$); the phase colored as gray represent spinel phase ($LiNi_{0.5}Mn_{1.5}O_4$).

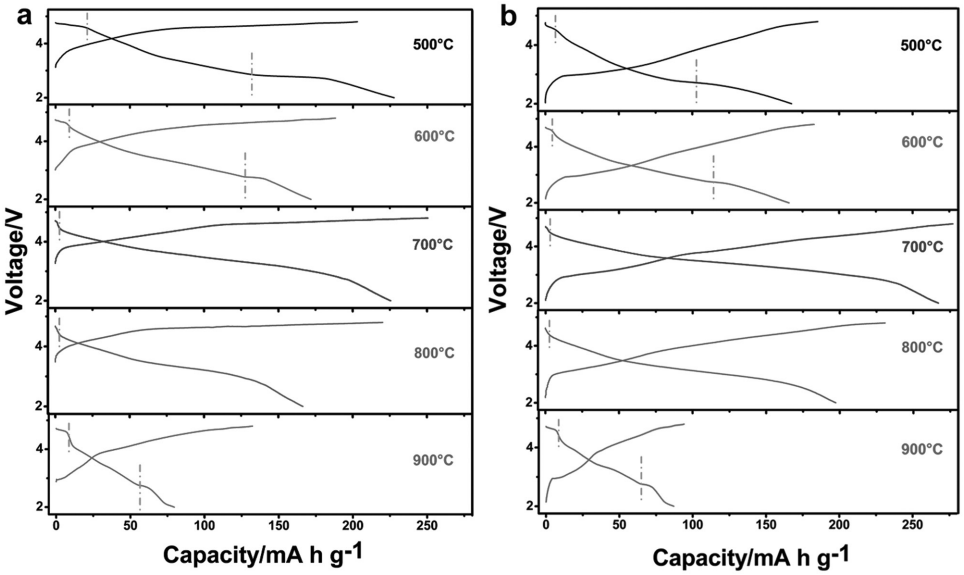

Figure 8. The a) first and b) fifth charge–discharge profiles of the products calcined at different temperatures in air for 12 h at a 0.1 C rate (1 C = 200 mA g^{-1}). The plateau of spinel phase is segregated by a dashed line.

crystallinity of spinel phase; there is no obvious reduction of the plateaus at 4.7 and 2.8 V.

Cycling tests were carried out at room temperature using a current rate of 0.2 C with the first five activation cycles at 0.1 C; the results are shown in **Figure 9**a. Both L-500 and L-600 suffer from rapid capacity decay in the first several cycles, and both of them maintain discharge capacities of about 50 mA h g^{-1} after 60 cycles at 0.2 C. As mentioned above, this capacity decay is explained by the loss of crystallinity of spinel phase during the repeated cycling processes. In addition, the inhomogeneous distribution of LLO and $LiNi_xMn_{2-x}O_4$ possibly induces lattice strains inside the particles, causing structural instability during the lithiation/delithiation process and leading to poor electrochemical reversibility of Li-excess layered cathode materials.[16] As mentioned before, the discharge capacities of both L-700 and L-800 increase in the first few cycles. When cycled at 0.2 C, L-700 demonstrates superior cyclic stability with 214 mA h g^{-1} remaining after 60 cycles while L-800 has only 72 mA h g^{-1} remained. This result is in agreement with the literature[22,23] that composites with certain content of spinel phase displayed the best properties. The improved cycling stability is benefited from the coating of proper content of spinel phase with minimized influence to the interior of the particles.[61] Although the discharge capacity is lower than other samples, L-900 has a stable cycling performance with 70% capacity retention at 0.2 C after 60 cycles. This cycling performance is benefited from the thick protection layer of $LiNi_xMn_{2-x}O_4$ with reduced capacity.[31]

The rate performances are compared in Figure 9b. Although the particle sizes are small, L-500 and L-600 demonstrate low capacity at high rate. The poor rate performance is probably due to the impact of amorphous spinel phase, which hinders the Li^+ transferring inside the particles. L-700 possesses much better rate property compared to other four samples, with discharge capacity of about 260 mA h g^{-1}

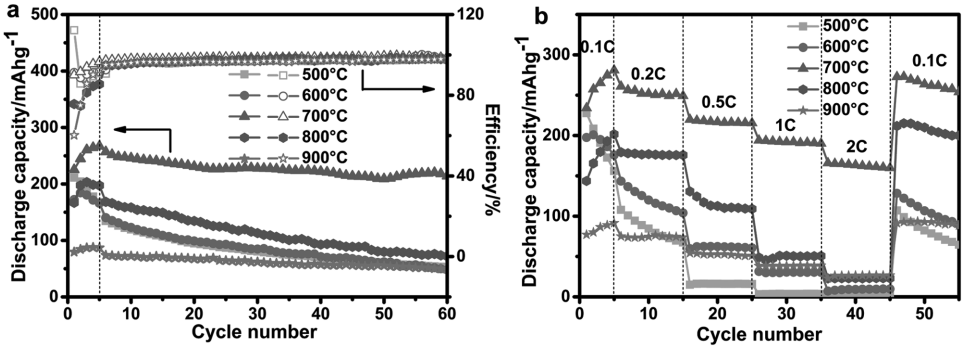

Figure 9. Cyclic performance and rate capability of the products calcined at different temperatures in air for 12 h. a) Plots of specific capacity versus cycle number for electrodes prepared with products calcined at different temperatures. Test conditions: cycle 1–5 at 0.1 C, cycle 6–60 at 0.2 C, voltage window: 2.0–4.8 V. b) Capacity retention of products calcined at different temperatures when cycling between 2.0 and 4.8 V at various rates from 0.1 to 2 C at room temperature.

at 0.2 C, 220 mA h g^{-1} at 0.5 C, 200 mA h g^{-1} at 1 C, and 170 mA h g^{-1} at 2 C, respectively. As mentioned in existing reports, this improvement is due to the introduction of a certain amount of spinel-like component, which will decrease the surface-film and charge-transfer resistances and thus improve the Li-ion diffusion coefficient.[22] Although the content of spinel phase slightly increased in L-800, L-800 exhibits poor rate property with discharge capacity of 23 mA h g^{-1} at 2 C, only 11% of its discharge capacity at 0.1 C. The substantially increased particle size of L-800 may be the major reason of this poor rate performance. Benefited by the porosity and high spinel content, L-900 has relative good rate property. At 2 C, the discharge capacity is 26 mA h g^{-1}, which is 30% of its discharge capacity at 0.1 C. The rate and cyclic performance of L-700 is compared with some outstanding works about LLO; as shown in Table S1 in the Supporting Information, the layered/spinel heterostructure in this work demonstrated a superior rate and cyclic performance.

Figure 10 presents the cyclic voltammetry (CV) curves of the calcination temperature-resolved samples. L-500 and L-600 manifest typical spinel redox peaks with two-step extraction/insertion process. The oxidation peaks at 4.7 V are associated with an overall electrochemical Ni^{2+}/Ni^{4+} couple, and the reduction peak at 2.8 V represents the spinel $Li[Ni_{0.5}Mn_{1.5}]O_4$ to rocksalt $Li_2[Ni_{0.5}Mn_{1.5}]O_4$ transformation as mentioned in the former section. Meanwhile, in the CV profile of L-600, a reduction peak referred to the Mn^{4+}/Mn^{3+} redox reaction in LLO[40,63] appears at around 3.3 V, indicating that the content of LLO increased in L-600 and offers more discharge capacity than that in L-500. Both L-700 and L-800 have wide oxidation peaks located from 3.7 to 4.5 V, presenting the Ni^{2+}/Ni^{4+} redox reactions;[64,65] the subsequent oxidation peaks between 4.5 and 4.8 V demonstrate the simultaneous lithium extraction and oxygen activation.[66] Beside that, there are still small reduction peaks at 2.8 V in the CV curves of L-700 and L-800, which are indicative of the existence of spinel phase. The CV profile of L-900 is similar to that of L-600, except for small redox peaks at about 4.0 V corresponding to Mn^{4+}/Mn^{3+} reaction in spinel phase, caused by the leaching out of $Li_xNi_{1-x}O$.[67,68] The slight shift of spinel redox peaks between each sample is also observed in former reports and may be associated with the different contents of spinel phase.[12]

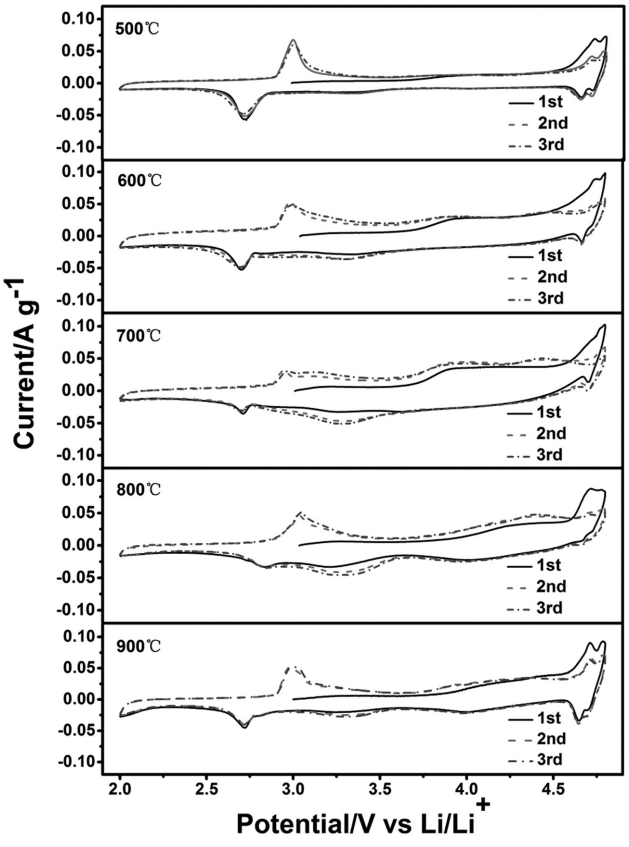

Figure 10. The first three cycles cyclic voltammograms of Li cells with the products calcined at different temperatures in air for 12 h. Measured at 25 °C with a scanning rate of 0.05 mV s^{-1}.

The relationship between the conductivities and the composition of cathode materials is studied by means of electrochemical impedance spectra (EIS) measurement. Figure S7 in the Supporting Information displayed the Nyquist plots of the electrodes made by products calcined at different temperatures after three cycles of charge–discharge. Prior to the measurements, all the cells were charged to 4.2 V to ensure identical status.[69,70] To quantitatively analyze the EIS results, an equivalent circuit was simulated by *Z*-view software, as shown as the inset of Figure S6 in the Supporting Information. R_b is the bulk resistance of the cell, R_s is the surface film resistance, R_{ct} is the charge-transfer resistance, C_s is the surface film capacitance, C_d is the double layer capacitance, and Z_w is the Warburg impedance associated with Li^+ diffusion in the material particles.[71] The values of simulated R_s and R_{ct} of all the samples are listed in **Table 1**. The R_{ct} of L-500 was found to be much higher than that of all other samples, indicating that L-500 has a much lower conductivity. That result is caused by the amorphization of spinel phase in the first three cycles. The minimum R_{ct} value of L-700 indicates a lower electrochemical polarization and better rate cycling performance with sample calcined at 700 °C for 12 h.

The electrochemical performance of layered/spinel heterostructured Li-rich materials seems to be rather different when calcined at various temperatures. Such differences may be attributed to the changing ratio of spinel to LLO phase and the leach out of rock salt phase, as well as the change of crystallinity and morphology. For example, L-600 and L-900 have a similar ratio of spinel to LLO phase, but the performances are quite different. In order to achieve layered/spinel heterostructure Li-rich materials with superior electrochemical properties, a proper method with optimized control of ratio of spinel to LLO phase and satellite phenomenon is necessary. Further exploration about the synergistic effect of the ratio of spinel to

Table 1. R_s, R_{ct} values of products calcined at different temperatures in air for 12 h after three cycles at 0.1 C and 25 °C.

	L-500	L-600	L-700	L-800	L-900
$R_s(\Omega)$	126.6	208.3	20.9	116.4	17.8
$R_{ct}(\Omega)$	868.7	416.3	151.0	241.7	382.9

LLO phase and the satellite phenomenon will be carried out in our future researches.

3. Conclusions

Layered/spinel heterostructure Li-rich materials were synthesized through a polyol method, and the influence of ratio of spinel to LLO phase and satellite phenomenon on samples' electrochemical performances has been systematically studied. The composites demonstrated diverse constitution when calcined at different temperatures, and electrochemical properties vary with the constitution changes. Based on the investigation of the crystal chemistry, oxidation state of the transition metal ions, and the thermal process, the formation of Li-rich layered materials was likely to go through a "Li-rich spinel phase decomposition" route. Satellite phenomena including the leach out of rock salt phase, and the change of crystallinity and morphology were observed during the phase transition; all the ratio of spinel to LLO phase and the satellite phenomenon synergistically affect the electrochemical performance of obtained composites. A specimen with superior electrochemical performance was obtained at 700 °C; the sample had a discharge capacity of 214 mA h g^{-1} remaining at 0.2 C after 60 cycles and discharge capacity of about 200 mA h g^{-1} at 1 C. The improved electrochemical performances were attributed to the proper content of spinel phase with minimized influence to the interior of the particles. This research is expected to inspire further development of well-designed layered/spinel heterostructured Li-rich materials with superior electrochemical performance.

4. Experimental Section

Synthesis of Layered/Spinel Composites: Layered/spinel heterostructured Li-rich materials, $Li_{1.2}Mn_{0.6}Ni_{0.2}O_2$ were synthesized by a polyol method that has been used in the preparation of $LiNi_{1/3}Co_{1/3}Mn_{1/3}O_2$.[72] Lithium acetate, manganese acetate tetrahydrate, nickel acetate tetrahydrate were used as the starting materials. All of these chemicals were purchased from Sigma-Aldrich Reagent were analytical reagent and used without any further purification. Lithium acetate, manganese acetate hydrate, and nickel acetate hydrate were added into 60 mL glycerol with molar ratios of 1.32: 0.6: 0.2. The solution was heated to 170 °C with a ramping rate of 5 °C min^{-1} under continuous stirring at 600 rpm min^{-1}. During the heating process, the solution color stepwise changed from green to earthy yellow, then pale yellow, and finally light green at 170 °C, demonstrating that the transition metals and lithium ions were successfully chelated by glycerol. After heating for 1 h, the solution was cooled to room temperature by water-cooling, and the obtained brown precipitates were collected by solvent evaporation at 125 °C. The as-prepared precipitate was ground and annealed in air with a ramping rate of 3.5 °C min^{-1}, first at 500 °C for 2 h, and then at different temperatures for 12 h to achieve the final products. The obtained products were washed with deionized water and ethanol several times, and finally dried in an oven at 60 °C for 4 h.

To obtain the controlled ratio of LLO to spinel phase and further investigate the mechanism of the formation of the layered/spinel heterostructure, the calcination temperatures were set as 500, 600, 700, 800, and 900 °C. The obtained products are labeled as L-500, L-600, L-700, L-800, L-900, respectively.

Materials Characterization: XRD patterns were recorded on Rigaku D/max-IIIB XRD at a voltage of 40 kV and a current of 40 mA, using Cu Kα radiation (λ = 0.15405 nm). The morphology and particle size of the specimens were characterized by SEM (FEI Sirion XL30) and transmission electron microscope (FEI Tecnai G2 F20). Thermogravimetric analysis (TGA) was performed on a TG instrument (Q50 TGA). XPS measurement was carried out on Thermo Fisher Scientific VG Kα Probe spectrometer. ICP analysis was carried out on inductively coupled plasma–optical emission spectrophotometer (Perkin Elmer Optima 8300), the specimens were dissolved in aqua regia with a concentration of 10 mg L^{-1}, and the content of elements were directly measured without any normalizing.

Electrochemical Measurement: The working electrode was made by mixing 75 wt% composite powders, 15 wt% Super P conductive carbon, and 10 wt% poly(vinylidene fluoride) in *N*-methyl-2 pyrrolidone. The mixture was ground and spread onto aluminum foil, and then dried in a vacuum oven at 110 °C for 10 h. The electrochemical measurements were carried out with CR2016 coin-type cells using Celgard 2400 membrane as separator. Both the counter and reference electrodes were lithium foils. The electrolyte (BASF) was composed of 1 M $LiPF_6$ solution in ethylene carbonate/dimethyl carbonate mixture solution (1:1 by volume). Land CT2001A battery test systems (LAND Wuhan Corp., China) was used for the galvanostatic charge/discharge cycle tests, and the potential ranged from 2 to 4.8 V at room temperature. Both the CV and EIS measurements were tested on an electrochemical workstation (CHI 660C, Shanghai Chenhua Instrument Corp., China). Two-electrode coin cell assembly was used to perform the CV data, the scan rate was 0.05 mV s^{-1} and tested at room temperature. EIS was carried out by applying an AC voltage of 5 mV over the frequency range of 0.01 Hz to 100 kHz.

Supporting Information

Supporting Information is available from the Wiley Online Library or from the author.

Acknowledgements

This work was financially supported in part by the National Science Foundation (NSF, DMR-1505902). Y.P., B.H., B.L., S.L., and Q.C. would like to thank the China Scholarship Council (CSC) for supporting their study as exchanging students in U.W. and UT Austin.

Received: August 23, 2016
Revised: November 10, 2016
Published online: January 4, 2017

[1] V. Etacheri, R. Marom, R. Elazari, G. Salitra, D. Aurbach, *Energy Environ. Sci.* **2011**, *4*, 3243.
[2] R. C. Massé, E. Uchaker, G. Cao, *Sci. Chin. Mater.* **2015**, *58*, 715.
[3] C. Liu, R. Massé, X. Nan, G. Cao, *Energy Storage Mater.* **2016**, *4*, 15.
[4] L. Song, S. Yang, W. Wei, P. Qu, M. Xu, Y. Liu, *Sci. Bull.* **2015**, *60*, 892.
[5] B. L. Ellis, K. T. Lee, L. F. Nazar, *Chem. Mater.* **2010**, *22*, 691.
[6] A. Manthiram, J. C. Knight, S. Myung, S. Oh, Y. Sun, *Adv. Energy Mater.* **2016**, *6*, 1501010.
[7] C. Liu, Z. G. Neale, G. Cao, *Mater. Today* **2015**, *2*, 109.
[8] J. C. Knight, P. Nandakumar, W. H. Kan, A. Manthiram, *J. Mater. Chem. A* **2015**, *3*, 2006.
[9] O. K. Park, Y. Cho, S. Lee, H. Yoo, H. Song, J. Cho, *Energy Environ. Sci.* **2011**, *4*, 1621.
[10] M. Wang, M. Yang, X. Y. Zhao, L. Q. Ma, X. D. Shen, G. Z. Cao, *Sci. Chin. Mater.* **2016**, *59*, 558.
[11] L. Wang, Z. Hu, K. Zhao, Y. Luo, Q. Wei, C. Tang, P. Hu, W. Ren, L. Mai, *Sci. Chin. Mater.* **2016**, *59*, 95.

[12] S.-H. Park, S.-H. Kang, C.S. Johnson, K. Amine, M. Thackeray, *Electrochem. Commun.* **2007**, *9*, 262.
[13] J. Cabana, S. Kang, C. S. Johnson, M. M. Thackeray, C. P. Grey, *J. Electrochem. Soc.* **2009**, *9*, A730.
[14] F. Wu, N. Li, Y. Su, H. Shou, L. Bao, W. Yang, L. Zhang, R. An, S. Chen, *Adv. Mater.* **2013**, *25*, 3722.
[15] F. Cheng, J. Chen, H. Zhou, A. Manthiram, *J. Electrochem. Soc.* **2013**, *10*, A1661.
[16] J. Zhao, R. Huang, W. Gao, J. Zuo, X. F. Zhang, S. T. Misture, Y. Chen, J. V. Lockard, B. Zhang, S. Guo, M. R. Khoshi, K. Dooley, H. He, Y. Wang, *Adv. Energy Mater.* **2015**, *5*, 1401937.
[17] H. Liu, D. Qian, M. G. Verde, M. Zhang, L. Baggetto, K. An, Y. Chen, K. J. Carroll, D. Lau, M. Chi, G. M. Veith, Y. S. Meng, *ACS Appl. Mater. Interfaces* **2015**, *7*, 19189.
[18] Q. Xia, X. Zhao, M. Xu, Z. Ding, J. Liu, L. Chen, D. G. Ivey, W. Wei, *J. Mater. Chem. A* **2015**, *3*, 3995.
[19] J. Liu, S. Wang, Z. Ding, R. Zhou, Q. Xia, J. Zhang, L. Chen, W. Wei, P. Wang, *ACS Appl. Mater. Interfaces* **2016**, *8*, 18008.
[20] Y. Zhao, J. Liu, S. Wang, R. Ji, Q. Xia, Z. Ding, W. Wei, Y. Liu, P. Wang, D. G. Ivey, *Adv. Funct. Mater.* **2016**, *26*, 4760.
[21] W. Li, L. Zeng, Y. Wu, Y. Yu, *Sci. Chin. Mater.* **2016**, *59*, 287.
[22] D. Luo, G. Li, C. Fu, J. Zheng, J. Fan, Q. Li, L. Li, *Adv. Energy Mater.* **2014**, *4*, 1400062.
[23] Y. Deng, F. Fu, Z. Wu, Z. Yin, T. Zhang, J. Li, L. Huang, S. Sun, *J. Mater. Chem. A* **2016**, *4*, 257.
[24] G. Wei, X. Lu, F. Ke, L. Huang, J. Li, Z. Wang, Z. Zhou, S. Sun, *Adv. Mater.* **2010**, *22*, 4364.
[25] S. Wang, Z. Lu, D. Wang, C. Li, C. Chen, Y. Yin, *J. Mater. Chem.* **2011**, *21*, 6365.
[26] L. Riekehr, J. Liu, B. Schwarz, F. Sigel, I. Kerkamm, Y. Xia, H. Ehrenberg, *J. Power Sources* **2016**, *325*, 391.
[27] J. Liu, J. Liu, R. Wang, Y. Xia, *J. Electrochem. Soc.* **2014**, *1*, A160.
[28] J. M. Paulsen, J. R. Dahn, *Chem. Mater.* **1999**, *11*, 3065.
[29] D. Mohanty, J. Li, D. P. Abraham, A. Huq, E. A. Payzant, D. L. Wood, C. Daniel, *Chem. Mater.* **2014**, *26*, 6272.
[30] Q. Zhong, A. Bonakclarpour, M. Zhang, Y. Gao, J. R. Dahn, *J. Electrochem. Soc.* **1997**, *144*, 205.
[31] C. Wang, K. A. Jarvis, P. J. Ferreira, A. Manthiram, *Chem. Mater.* **2013**, *25*, 3267.
[32] J. Liu, M. Hou, J. Yi, S. Guo, C. Wang, Y. Xia, *Energy Environ. Sci.* **2014**, *7*, 705.
[33] Y. Gao, J. R. Dahn, *J. Electrochem. Soc.* **1996**, *5*, 1783.
[34] Y. Huang, X. Hou, X. Fan, S. Ma, S. Hu, K. H. Lam, *Electrochim Acta* **2015**, *182*, 1175.
[35] M. L. Castelló, J. Dweck, D. A. G. Aranda, *J. Therm. Anal. Calorim.* **2009**, *97*, 627.
[36] W. Yan, Y. Liu, S. Guo, T. Jiang, *ACS Appl. Mater. Interfaces* **2016**, *8*, 12118.
[37] Y. Zhao, Y. Sun, Y. Yue, X. Hu, M. Xia, *Electrochim. Acta* **2014**, *130*, 66.
[38] Y. Xiang, Z. Yin, Y. Zhang, X. Li, *Electrochim. Acta* **2013**, *91*, 214.
[39] W. Chen, Y. Song, C. Wang, Y. Liu, D. T. Morris, P. A. Pianetta, J. C. Andrews, H. Wu, N. Wu, *J. Mater. Chem. A* **2013**, *1*, 10847.
[40] M. Chen, X. Xiang, D. Chen, Y. Liao, Q. Huang, W. Li, *J. Power Sources* **2015**, *279*, 197.
[41] H. Duncan, B. Hai, M. Leskes, C. P. Grey, G. Chen, *Chem. Mater.* **2014**, *26*, 5374.
[42] S. Shi, T. Wang, M. Cao, J. Wang, M. Zhao, G. Yang, *ACS Appl. Mater. Inter.* **2016**, *8*, 11476.
[43] L. Li, X. Zhang, R. Chen, T. Zhao, J. Lu, F. Wu, K. Amine, *J. Power Sources* **2014**, *249*, 28.
[44] E. Beyreuther, S. Grafstrom, L. M. Eng, C. Thiele, K. Dorr, *Phys. Rev. B* **2006**, *73*, 155425.
[45] M. Chen, D. Chen, Y. Liao, X. Zhong, W. Li, Y. Zhang, *ACS Appl. Mater. Interfaces* **2016**, *8*, 4575.
[46] K. Luo, M. R. Roberts, R. Hao, N. Guerrini, D. M. Pickup, Y. Liu, K. Edström, J. Guo, A. V. Chadwick, L. C. Duda, P. G. Bruce, *Nat. Chem.* **2016**, *8*, 684.
[47] L. Simonin, J. Colin, V. Ranieri, E. Canevet, J. Martin, C. Bourbon, C. Baehtz, P. Strobel, L. Daniela, S. Patoux, *J. Mater. Chem.* **2012**, *22*, 11316.
[48] F. Wu, J. Tian, Y. Su, J. Wang, C. Zhang, L. Bao, T. He, J. Li, S. Chen, *ACS Appl. Mater. Interfaces* **2015**, *7*, 7702.
[49] B. Song, Z. Liu, M. O. Lai, L. Lu, *Phys. Chem. Chem. Phys.* **2012**, *14*, 12875.
[50] J. Dupin, D. Gonbeau, P. Vinatier, A. Levasseur, *Phys. Chem. Chem. Phys.* **2000**, *2*, 1319.
[51] T. R. Penki, D. Shanmughasundaram, A. V. Jeyaseelan, A. K. Subramani, N. Munichandraiah, *J. Electrochem. Soc.* **2013**, *1*, A33.
[52] D. Wang, R. Yu, X. Wang, L. Ge, X. Yang, *Sci. Rep.-UK* **2015**, *5*, 8403.
[53] S. Duraisamy, T. R. Penki, M. Nookala, *New J. Chem.* **2016**, *40*, 1312.
[54] J. Meng, S. Zhang, X. Wei, P. Yang, S. Wang, J. Wang, L. Honglei, X. Yalan, L. Guanrao, *RSC Adv.* **2015**, *5*, 81565.
[55] C. S. Johnson, N. Li, C. Lefief, J. T. Vaughey, M. M. Thackeray, *Chem. Mater.* **2008**, *20*, 6095.
[56] X. Yang, J. McBreen, W. Yoon, C. P. Grey, *Electrochem. Commun.* **2002**, *4*, 649.
[57] K. Li, F. Shua, J. Zhang, K. Chen, D. Xue, X. Guo, S. Komarneni, *Ceram. Int.* **2015**, *41*, 6729.
[58] R. Wang, X. He, L. He, F. Wang, R. Xiao, L. Gu, H. Li, L. Chen, *Adv. Energy Mater.* **2013**, *3*, 1358.
[59] S. Han, B. Qiu, Z. Wei, Y. Xia, Z. Liu, *J. Power Sources* **2014**, *268*, 683.
[60] P. K. Nayak, J. Grinblat, M. D. Levi, O. Haik, E. Levi, M. Talianker, B. Markovsky, Y. Sun, D. Aurbach, *Chem. Mater.* **2015**, *27*, 2600.
[61] D. Ye, K. Ozawa, B. Wang, D. Hulicova-Jurcakova, J. Zou, C. Sun, L. Wang, *Nano Energy* **2014**, *6*, 92.
[62] D. Ye, B. Wang, Y. Chen, G. Han, Z. Zhang, D. Hulicova-Jurcakova, J. Zou, L. Wang, *J. Mater. Chem. A* **2014**, *2*, 18767.
[63] J. R. Croy, K. G. Gallagher, M. Balasubramanian, B. R. Long, M. M. Thackeraya, *J. Electrochem. Soc.* **2014**, *3*, A318.
[64] P. Oh, M. Ko, S. Myeong, Y. Kim, J. Cho, *Adv. Energy Mater.* **2014**, *4*, 1400631.
[65] Y. X. Wang, K. H. Shang, W. He, X. P. Ai, Y. L. Cao, H. X. Yang, *ACS Appl. Mater. Interfaces* **2015**, *7*, 13014.
[66] Q. Li, G. Li, C. Fu, D. Luo, J. Fan, D. Xie, L. Li, *J. Mater. Chem. A* **2015**, *3*, 10592.
[67] Y. Qian, Y. Deng, Z. Shi, Y. Zhou, Q. Zhuang, G. Chen, *Electrochem. Commun.* **2013**, *27*, 92.
[68] X. Fang, M. Ge, J. Rong, C. Zhou, *J. Mater. Chem. A* **2013**, *1*, 4083.
[69] B. Huang, X. Li, Z. Wang, H. Guo, X. Xiong, J. Wang, *J. Alloy Compd.* **2014**, *583*, 313.
[70] K. Zhang, Z. Hu, Z. Tao, J. Chen, *Sci. Chin. Mater.* **2014**, *57*, 42.
[71] Y. Deng, S. Zhao, Y. Xua, C. Nan, *J. Mater. Chem. A* **2014**, *2*, 18889.
[72] J. Li, R. Yao, C. Cao, *ACS Appl. Mater. Interfaces* **2014**, *6*, 5075.